Construction and Building Materials 439 (2024) 137285

Contents lists available at ScienceDirect

Construction and Building Materials

journal homepage: www.elsevier.com/locate/conbuildmat

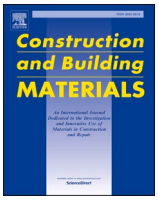

Activation of ground granulated blast-furnace slag with calcium hydroxide nanoparticles towards the consolidation of adobe

Monica Tonelli, Rachel Camerini, Piero Baglioni, Francesca Ridi *

Department of Chemistry "Ugo Schiff" and CSGI, University of Florence, via della Lastruccia 3, 50019 Sesto Fiorentino, Florence, Italy

ARTICLE INFO

Keywords:
Low carbon cements
Calcium silicate hydrate
Nano-lime
Slag activator
Earthen-based materials

ABSTRACT

Adobe earthen materials, one of the oldest and most widespread forms of construction, are easily susceptible to degradation due to their porous structure and variable composition. Effective consolidation treatments should involve compatible materials and allow for a good penetration, to restore grains cohesion. Among all possible alternatives for the restoration of earthen masonry, the formation *in-situ* of calcium silicate hydrate has been reported as a compatible and efficient solution. In this study we report the investigation of consolidation treatments based on ground granulated blast furnace slag (a secondary raw material from steel production) activated with calcium hydroxide, either as bulk or nanometric particles, to allow for the consolidation of porous structures through the formation of calcium silicate hydrate. Different dispersions were thoroughly characterized, and the best formulation was applied on adobe mock-up samples. The effect of the treatment revealed that calcium hydroxide nanoparticles, synthesized through an easy and convenient process, can accelerate the activation of the slag and increase the formation of the cementitious binder, both on the surface of the treated substrates, and into their porous matrix. These results pave the way towards the use of nano-sized alkali activators to boost the hydration of geopolymers.

1. Introduction

Adobe represents one of the most popular earthen masonry materials [1,2], widely diffused worldwide both in the architectural contest and in the artistic field, despite its high susceptibility to weathering [3]. Adobe bricks are handmade silicate-based materials, produced by mixing earth and water to a plastic consistency, eventually including some reinforcement fibers (sticks, straw, dung), mold casting the mixture, and letting the water evaporate by sun drying and curing. Although there is no universal recipe as their preparation varies according to local availability and traditions, typically the clay fraction mainly consists of alumino-silicates, carbonates, sulfates and oxides, while the granular soils (sand and gravel) represent the inert fraction and play an important role in controlling the mixture workability and shrinkage [4]. The final porosity, which in turns affects the mechanical properties, strongly depends on the cohesive soil fraction and granulometry, and can range from micrometer to millimeter scale, making the structure easily susceptible to degradation [5,6]. The prolonged action of wind and water erosion leads to the progressive reduction of grain's cohesion, loss of mechanical properties, and eventually cracking and crumbling. The damages involve the upper surface, progressively exposing the underlying layers to atmospheric agents. Effective consolidation treatments must entail compatible materials and provide a good penetration and renewal of grains cohesion, but many of the traditional products (alkoxysilanes, synthetic or natural polymers) lack of either physico-chemical compatibility or effectiveness [7–9]. It is worth mentioning here that, despite the high susceptibility and wide diffusion of adobe, there is no universally recognized standard for the reinforcement of earthen masonry.

The use of calcium silicate hydrate, $((CaO)_y\text{-}(SiO_2)\text{-}(H_2O)_x$, C-S-H), the main binding phase that is responsible for the mechanical properties of cementitious materials [10], has been already explored in the cultural heritage field for consolidation treatments. Impregnation products able to produce C-S-H gel *in-situ* have been reported in the literature for the reinforcement of different damaged porous substrates, including earthen materials, stones, ceramics, and cementitious materials themselves [3,11,12]. Nowadays, various cementitious materials are under investigation as alternative binders, or as supplementary cementitious materials

Abbreviations: C-S-H, Calcium Silicate Hydrate; GGBS, Ground Granulated Blast-furnace Slag; CH, Calcium Hydroxide; AC, Abrasion Coefficient; DI, Decohesion Index; XRD, X Ray Diffraction; FT-IR, Fourier Transform Infrared spectroscopy; SEM, Scanning Electron Microscopy; SM, Supplementary Material; TP, Total Porosity.

* Corresponding author.
E-mail address: francesca.ridi@unifi.it (F. Ridi).

https://doi.org/10.1016/j.conbuildmat.2024.137285
Received 16 February 2024; Received in revised form 26 June 2024; Accepted 27 June 2024
Available online 11 July 2024

to partially replace Portland cement, whose production is associated with large CO_2 emissions [13]. To this purpose, the use of industrial byproducts has been crucial for the development of sustainable cementitious materials, towards the reduction of greenhouse gasses' emissions, as required by the tangible climate changes claiming for urgent actions [14,15]. Among the wastes used in view of their pozzolanic properties, Ground Granulated Blastfurnace Slag (GGBS), a glassy byproduct of pig iron and steel production, is particularly interesting [16]. Today, GGBS is mainly used in blended cements, but it finds applications also for the stabilization of clays. In particular, GGBS has been already reported for the preparation of sustainable unfired clay building bricks enriched with C-S-H binder, prepared using CaO/GGBS/clay mixtures [17–19]. This slag has a chemical composition similar to that of Portland cement, being mainly composed by CaO, MgO, Al_2O_3 and SiO_2, and, when finely ground [20,21], it reacts with water to form C-S-H [20,22,23]. Although GGBS displays cementitious properties and hardens in the presence of water, due to its glassy nature its hydration with sole water is very slow, and thus some activators are necessary to boost the hydration rate [24]. At the same time, the composition of GGBS can be very variable, depending on the starting raw materials used into the blast furnace, which in turn influences the hydraulic activity of the slag. The use of Portland cement or alkalis as GGBS activators is a well-recognized method to speed up the reaction rate, promoting the slag reactivity by increasing the pH of the system [13] Among all possible activators, we can find various hydroxide based strong alkali, (NaOH, $Ca(OH)_2$, KOH), silicate-based activators, acid salts, aluminates-based activators, oxide-based activators and aluminosilicates-based activators [24,25]. The main role of these activators relies on controlling the pH, to prevent long setting times and to favour the formation of C-S-H, which cannot form when pH is below 9.5 [26]. According to the hypotheses reported in the literature, a thin layer of silica gel forms on the surface of GGBS particles upon hydration, preventing further reaction with water. The presence of strong alkalis, such as $Ca(OH)_2$, hereinafter CH, favors the dissolution of this surface layer, fostering the precipitation of hydration products (C-S-H), as illustrated in Fig. 1 [24,27].

In the literature, the hydration process of GGBS is typically accelerated by using bulk activators, such as CH, while the effect of alkali activators in the form of nanoparticles was never investigated so far, even though it could be possible to exploit the high reactivity of such nanoparticles, arising from the high surface area to volume ratio [28,29]. For example, it has been already demonstrated that non-aqueous dispersions of kinetically stable CH nanoparticles (nano-lime) can be used to reinforce murals [30], exploiting the effect of the reduced size of the particles on their reactivity, stability, and ability to penetrate through porous matrices [31–33]. These systems already find application in the field of restoration. In fact, over the last three decades, nanotechnology has strongly contributed to the development of promising solutions for the protection and consolidation of various substrates, and nowadays dispersions of alkaline-earth metal hydroxide nanoparticles are among the best systems available for consolidation of cultural heritage carbonate materials [11]. Some of the authors also recently demonstrated that a combination of CH nanoparticles and nanosilica can be used to accelerate the precipitation of C-S-H, successfully employed for the consolidation of earthen masonry [3,34].

In this study, we explored the possibility of reinforcing adobe through the precipitation of C-S-H binder gel phase from aqueous diluted suspensions of GGBS activated with calcium hydroxide, either bulk or nano-sized. Thus, further steps with respect to the mentioned recent advancements are represented by: *i*) the employment of a byproduct for the development of environmentally sustainable formulations to be used for the consolidation of porous substrates, allowing to extend the life of vulnerable adobe constructions; *ii*) the use of nano-sized alkali activators to boost the hydration of geopolymers. To assess the effect of the particles' size on the effectiveness of C-S-H precipitation, different formulations were prepared either using nanometric or bulk CH activator, together with fine GGBS. Nano-lime particles were synthesized [35,36] and used either as an ethanol dispersion or dried. All samples were thoroughly characterized by monitoring the pH evolution over time and through X-Ray Diffraction (XRD), Fourier Transform Infrared spectroscopy (FT-IR), and Scanning Electron Microscopy (SEM). One of the dispersions was then selected for applications on adobe mock-up samples, to assess its efficacy on the consolidation of such weathering susceptible materials. Treated samples were thus characterized by means of 2D Confocal Raman mapping to confirm the *in-situ* formation of C-S-H binder gel phase. The efficacy of the treatment in preventing the typical dusting of adobe was evaluated through peeling and abrasion tests, and the penetration of the consolidation treatment into the substrate was investigated by means of X-Ray microtomography.

2. Materials and methods

2.1. Materials

A fine grade GGBS (CaO ≈ 41 %, SiO_2 ≈ 35.7 %, Al_2O_3 ≈ 11.6 %, MgO ≈ 8.7, %, TiO_2 ≈ 0.6 %, SO_3 ≈ 0.3 %) was kindly provided by Ecocem ltd (d_{10} = 1.24 μm, d_{50} = 5.98 μm, d_{90} = 19.7 μm; measurements were performed by means of a Mastersizer 3000 laser diffraction particle size analyser, Malvern). Calcium hydroxide powder (96 %,

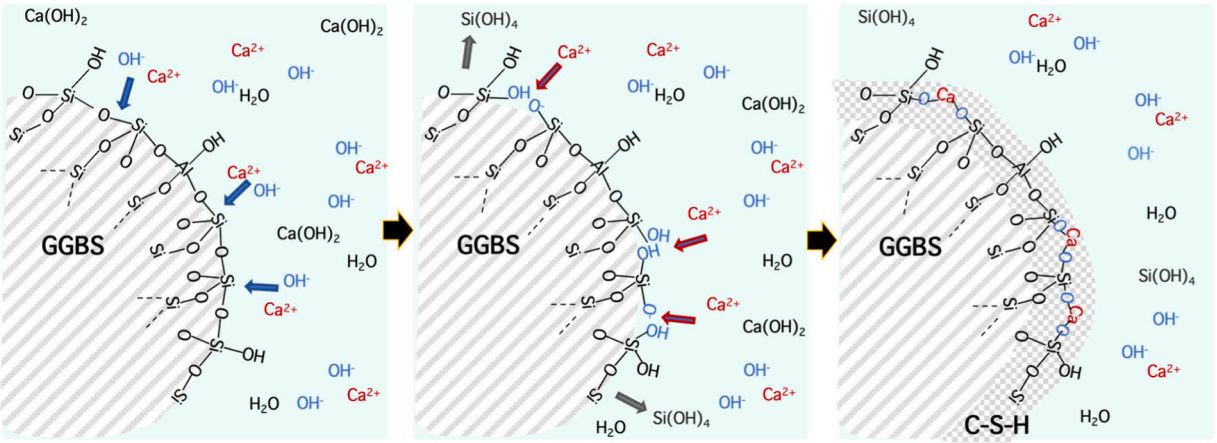

Fig. 1. Schematic design of the hydration process of GGBS in the presence of CH activator. GGBS is a latent cementitious material, and the hydration is a three-stage process: 1) the slag particles are coated by impermeable aluminosilicate hydrates, 2) the hydroxide ions break down this layer and activate the slag hydration, Ca^{2+} diffuse inside and silicate anions are released, 3) the pozzolanic reaction takes place and C-S-H forms.

Merck) was used as received. CH nanoparticles were synthesized following a procedure reported in the literature [35,36], using metal granular calcium (Aldrich, 99 %) and ethanol absolute (Sigma-Aldrich, 99.8 %), by a one-pot reaction in a high-pressure reactor consisting of two steps:

$$Ca + Ethanol \rightarrow Ca(ethoxide)_2 + H_2 \quad (1)$$

$$Ca(ethoxide)_2 + H_2O \rightarrow Ca(OH)_2 + Ethanol \quad (2)$$

The synthesis yields an ethanol dispersion of hexagonal platelets of about 100 nm (portlandite), which were either used as a suspension or as dry powder. For the drying process, the nanoparticles were heated at 80 °C under nitrogen flow until the ethanol was completely removed, and they were then characterized by means of SEM to confirm their nanometric size and through gas porosimetry to determine the specific surface area, SSA. The measurement was performed by means of a 3Flex gas porosimeter (Micromeritics, Norcross, GA, USA), using nitrogen as adsorptive gas. Before the measurements, the dried samples were outgassed for 60 min at 70 °C under nitrogen flow with a FlowPrep apparatus, and then tested for the adsorption of N_2. The measured SSA resulted 30 m^2/g.

From the specific surface area, the average size of CH nanoparticles was estimated by calculating the equivalent spherical diameter, or BET particle diameter: $d_{BET} = 6/(q^*S_w) = 90$ nm, where q is the density of CH (2.21 g/cm^3) and S_w is the specific surface area.

Water was purified by a Millipore Milli-Q UV system (resistivity > 18 MΩcm).

KBr (FT-IR grade, Merck) for FT-IR analyses was used as received.

2.2. Preparation of the formulations

Four formulations containing micro-sized and nano-sized CH and GGBS were prepared in glass vials, as described in Table 1. After a series of preliminary tests, the proper concentrations of GGBS and CH were selected, to grant a sufficient amount of SiO_2 and a proper alkaline activator percentage. The resulting silicon/calcium hydroxide ratio in the freshly prepared formulations is about 7. CH nanoparticles were used both as EtOH dispersions, *i.e.*, as synthesized, or after drying. As a comparison, also bulk calcium hydroxide was either employed dried or dispersed in EtOH. A water to solid ratio (W/S) of 40 by mass was chosen to enable the application of the formulations on artistic substrates and their easy penetration through the porosities. GGBS_npCH* and GGBS_CH* formulations were prepared by mixing GGBS and CH as dry powders with water. GGBS_npCH and GGBS_CH formulations were prepared by adding the ethanol dispersion of CH into the GGBS water dispersion. All the systems were sonicated for 10 min after mixing the components.

2.3. Characterization of the formulations

2.3.1. pH measurements

The pH was tested on the water-based samples immediately after preparation and then monitored with time, to ensure that these the formulations displayed the proper alkalinity for the GGBS to be activated [26,37]. pH measurements were performed on the supernatant solutions, following a method previously described in the literature for the investigations of different cement mixtures [15,38,39]. In a polyethylene flask we poured about 5 mL of the freshly prepared formulations. The container was sealed and constantly shaken in an orbital stirrer. Then, at selected time intervals (0, 1, 3, 7, 14, 28 days), the samples were centrifuged at 7500 rpm for 5 min to precipitate the powders, and the pH of the supernatant solutions was measured at 25 °C using a BASIC 20 Crison pH meter. The pH of a dispersion of GGBS in H_2O was also measured as reference. After the measurement, the samples were redispersed again by means of a vortex.

Table 1
Composition of the investigated formulations.

FORMULATION NAME	Alkaline activator	$Ca(OH)_2$ conc. (g/L)	GGBS conc. (g/L)	W/S ratio	EtOH/S ratio
*GGBS_npCH**	np $Ca(OH)_2$	1.3	25	40	-
*GGBS_CH**	bulk Ca $(OH)_2$, Merck	1.3	25	40	-
GGBS_npCH	np $Ca(OH)_2$	1.05	20	40	10
GGBS_CH	bulk Ca $(OH)_2$, Merck	1.05	20	40	10

2.3.2. X-Ray diffraction

X-ray diffractograms were recorded using a D8 Advance (Bruker) with DAVINCI design, using a Cu source (emitting radiation λ=1.54 Å) and operating at 40 kV and 40 mA. Data were collected on all formulations in the 5–70° 2θ range, using an increment of 0.04° and a time per step of 0.3 s. To stop the hydration reaction, after 1, 7, and 28 days from the preparation, roughly 1 mL of all dispersions was withdrawn and freeze-dried. Peaks' assignment was based on the Powder Diffraction Files (PDF) of the database of the International Centre for Diffraction Data.

2.3.3. Fourier transform infrared spectroscopy

To stop the hydration reaction, roughly 1 mL of all dispersions was withdrawn and freeze-dried soon after preparation (0 days) or after 1, 3, 7, and 28 days of curing. FT-IR spectra were collected using a Cary 670 FT-IR instrument (Agilent Technologies), in transmittance mode, acquiring 128 scans for each measurement, in the spectral range of 4000–400 cm^{-1}, with a spectral resolution of 2 cm^{-1}, and a delay time of 30 s. To allow a semi-quantitative evaluation of C-S-H production from the alkaline activation of GGBS, the analyses were performed using KBr pellet method. 200 mg KBr pellets containing 1 % of each freeze-dried grinded powder were prepared, after drying KBr overnight under vacuum at 130 °C. The spectrum of pristine GGBS was also collected. Background spectra were collected prior to each measurement. The obtained spectra were deconvoluted via multipeak fitting analysis in the spectral region between 730 and 1330 cm^{-1}, with Gaussian functions and a linear baseline, using Igor Pro Software (version 9.01, Wavemetrics Inc.), to monitor the silicate chain growth by looking at the evolution of the relative abundances of Q_n species in the hydrating slag, where n refers to the number of bridging oxygen atoms in the silicate systems.

2.3.4. Scanning electron microscopy

After 1, 7, and 28 days from the preparation, roughly 1 mL of all dispersions was withdrawn and freeze-dried to stop the hydration reaction. FE-SEM images were acquired on dry powders using a field-emission ΣIGMA microscope (Carl Zeiss Microscopy). Images were collected using the InLens detector, with an accelerating potential of 2.00 kV, at a working distance of ~ 4 mm.

2.4. Application on mock-up samples

After the characterization of the four systems, one formulation was selected and used for consolidation tests on a porous substrate of artistic, architectural, and archaeological interest. Handmade adobe bricks from a contemporary construction site of the Morelos state (Mexico) were selected and used to prepare samples with approximate dimensions of 3x3x1.5 cm^3 and weight of ~15–20 g. Granulometric analysis on adobe bricks collected from the same site were classified as silty sands with low clay percentage, according to the Unified Soil Classification System (USCS). Soils from the Morelos region are indeed granular soils, with a low cohesive fraction responsible for the low mechanical properties of

the samples. The samples were prepared in two ways, *i.e.,* by cutting an original adobe brick from the Morelos state (Mexico) into smaller pieces, or by grinding the original brick and mixing the obtained soil with water, mold-casting the mixture, and curing it for 1 month. In the first case, irregular samples with the same physico-chemical properties of the original adobe were obtained (see also Figure S1A in the Supplementary Material, SM): these samples were used for X-ray micro computed tomography and peeling test. In the second case, the grinding step produced a fine and homogeneously mixed powder that returned more regularly shaped and less rough mock-ups (Fig. S1B in the SM), suitable for Raman mapping and abrasion test. All adobe mock-ups were treated by drop-casting the formulation (about 3 mL) onto the upper sample's surface (about 9 cm^2), and air cured for 28 days.

2.5. Characterization of mock-up samples

2.5.1. 2D Confocal Raman mapping

Confocal Raman microscopy was carried out to investigate the formation of C-S-H binder on the treated earthen samples, in order to confirm that the hydration reaction properly proceeds also when the GGBS/CH formulations are applied on degraded substrates and the hardening occurs *in-situ*. Raman analysis and mapping were performed with a Renishaw inVia Qontor confocal MicroRaman system. The instrument was equipped with a 532 nm laser (Nd:YAG solid state type, 50 mW, 1800 l/mm grating), front illuminated CCD camera and research-grade Leica DM 2700 microscope equipped with a 50 X objective (theoretical spot size 1.3 μm). Raman maps were collected in the spectral range 150–1900 cm^{-1}, with an exposure time of 1 s, 1 accumulation, and using a step size of 2 μm. Spectra were processed with the Renishaw software WiRE™, corrected for cosmic rays, baseline and noise, and then used to obtain maps. Different maps were collected in different regions of the surface. As a reference, the spectrum of pure dried CH nanoparticles, adobe and GGBS were also collected.

2.5.2. X-Ray micro computed tomography

X-ray microtomography was performed with a SKYSCAN 1172 high-resolution μCT scanner (Bruker) on adobe samples, before and after the consolidation treatment, to evaluate the penetration of the treatment and estimate the porosity variation. Experiments were performed at 100 kV and 100 μA, at 10 W and using an Al/Cu filter, with a step size of 0.1, allowing for a theoretical resolution of ~ 13 μm. Image processing and porosity calculation were performed with the NRecon Reconstruction Program software 1.7.4.6. For the total porosity, a volume of interest was selected and used for both the 3D and 2D analyses, after tomography reconstruction. Pristine and treated images were also compared through overlapping with Data Viewer software 1.5.6.2, allowing to highlight the differences between the reconstructions.

2.5.3. Abrasion test

Abrasion tests were performed on pristine and treated samples to evaluate the surface resistance to mechanical erosion, following a standardized procedure developed for compressed earth blocks [40,41], adapted for our adobe samples. The test consists of brushing the block surface at constant pressure, using a metal brush with a constant mass on the top center of it. The mass used for compressed earth blocks was reduced from 3 to 1 Kg for testing adobe. Each brushing cycle consists of 60 rounds of brushing per minute, and the ratio of the surface to the quantity of the material removed gives the abrasion coefficient (AC, cm^2/mg), proportional to the abrasion resistance. For the calculation of the AC, two brushing cycles were repeated on the same area, to get information on the cohesion properties of progressively deeper layers, and the data here reported are the average of three tests.

2.5.4. Peeling test

Peeling tests were performed to evaluate the surface cohesion properties, by pressing and then peeling off pieces of adhesive tape of specific weight and area from the samples' surface [42]. The weight of the material detached per unit area gives the decohesion index (DI, mg/cm^2), which is inversely proportional to the grains' cohesion forces. The data here reported are the average of three measurements, performed on three different areas of the samples.

3. Results and discussion

3.1. Characterization of the formulations

In order to ensure the achievement of the right pH to favor the activation of GGBS and precipitation of C-S-H, the pH of the two water based formulations was monitored for 28 days (see Fig. 2). As already well established, pH plays a major role in the hydration of GGBS towards the precipitation of C-S-H binder gel phase. It has been reported that C-S-H cannot form when pH is below 9.5 [43–45], and the dependence of C-S-H composition and formation rate on pH conditions has been largely investigated in the literature [25,37,45–47]. In very alkaline conditions silica is strongly ionized and at pH > 11.5 it starts to solubilize [44,48]. At the same time, calcium hydroxide can buffer the solution at pH ≈ 12.5 ($Ca(OH)_2$ pKa ≈ 12.5 [49]), providing optimal condition for an efficient formation of C-S-H.

According to the results reported in Fig. 2, all the investigated formulations display a pH higher than 12 in the entire investigated period, confirming the proper pH to activate the hydration of the slag by enhancing the solubility of the water impermeable layer typically forming on the surface of GGBS particles (Fig. 1). Looking at Fig. 2, we can see that the pH slightly decreases during the first week of hydration from 12.4 to 12.2, and then raises again to about 12.4, reaching a plateau. This trend could be attributed to the combination of different factors: *i*) OH^- are released from calcium hydroxide, that is mostly solubilized in the investigated samples soon after preparation, being way below its solubility point ($K_{sp} = 4.7 \times 10^{-6}$ at 25°C [50]); *ii*) OH^- activates GGBS by breaking the Si-O-Si network of the impermeable layer of silicates that is present on the surface of the slag particles (see also Fig. 1), the concentration of hydroxide ions slightly decreases and so does the pH; *iii*) the generated $HSiO_3^-/SiO_3^{2-}$ species react with Ca^{2+} and C-S-H precipitates upon reaction between silanols and Ca^{2+}; *iv*) part of unreacted CaO contributes to the increase of the pH after one week, through the equilibrium $CaO + H_2O \longrightarrow Ca^{2+} + 2OH^-$ [44,51]; *v*) C-S-H dissolution and reprecipitation equilibria stabilize the pH above 12, as previously observed for C-S-H gels of Ca/Si molar ratio > 1 [43,50]. In the last stage of the curve the pH is mostly regulated by C-S-H dissolution, as the presence of $Ca(OH)_2$ can be safely excluded considering also the results of the XRD and FT-IR experiments reported below. Thus, we can hypothesize that the forming binder gel could be well described by a Ca/Si ratio of about 1.2, associated to a pH ≈ 12 [50].

It is worth noting that the presence of CH in the form of nanoparticles (sample GGBS_npCH*), leads to a slightly lower pH in the first days of hydration (see Fig. 2). We can infer that the use of nano-CH, exposing a

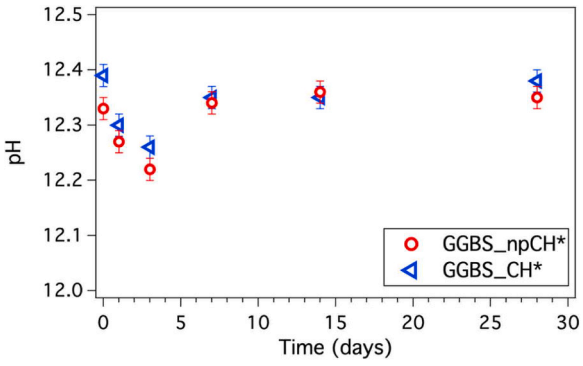

Fig. 2. pH evolution during setting of the investigated formulations.

larger surface area than bulk calcium hydroxide, accelerates the reactions occurring in the system. In fact, it is reasonable to assume that the hydroxide ions, quickly released from the nanoparticles, are promptly consumed by the reaction with GGBS, fastening the decrease of OH^- associated with their consumption upon activation of the slag. This hypothesis is also supported by FT-IR experiments reported below, that indicate a lower amount of portlandite in GGBS_npCH* than in GGBS_CH* in the formulations characterized soon after preparation, *i.e.*, when C-S-H is still scarce (see also XRD results) and the pH depends on two compelling processes: calcium hydroxide dissolution (OH^- release) and GGBS activation (OH^- consumption). As a result, the use of nanoparticles boosts the activation of GGBS and the formation of C-S-H, as confirmed also from FT-IR and XRD analyses.

The pH of a dispersion of GGBS in water in absence of calcium hydroxide was measured as reference, using the same concentration of the investigated formulations, and resulted to be about 10, confirming the need of an alkali activator.

XRD analysis (see Fig. 3) was performed on the investigated samples at different times of hydration, to gain information on the effect of different alkaline activation conditions. In all formulations we observe an evolution of the diffraction curves with time. The broad signal at ~ 30° arising from GGBS (see also the curve of pure GGBS reported in Fig. S2 in the SM) decreases with time, as it is consumed by the hydration reaction. At the same time, the signals ascribed to portlandite (18.0°, 34.1°) [44,52] decrease with time. Meanwhile, different peaks characteristic of C-S-H appear and increase with time (peaks at 2θ values of 29.1°, 31.8°, and 49.8°) [52–55]. The presence of some calcium carbonate (peaks at 23.1°, 29,4°, 39.3°, and 48.6°) can be explained by considering a partial carbonation of CH due to air exposure [56]. Other signals are also present, ascribable to aluminate phases and to their hydration reactions: hemicarboaluminate (21.5°) [23], and calcium aluminate phases, like hydrogarnet (20.0°) [57–60]. Overall, the main phase present at 28 days of reaction in all samples is tobermorite-like C-S-H. The comparison among the different formulations shows that in absence of EtOH (Fig. 3A and C) the precipitation of C-S-H occurs faster than in the presence of ethanol (Fig. 3B and D). Moreover, when using CH nanoparticles (Fig. 3C and D) the hydration reaction is boosted more than in the presence of bulk CH (Fig. 3A and B), allowing a faster formation of abundant C-S-H.

Despite that, when using nano-$Ca(OH)_2$ a very small signal at 18.0°, associated with portlandite, is still present after 28 days of hydration. Thus, the hydration kinetics of GGBS upon CH activation was further monitored through FT-IR analysis, to better understand the difference among the samples, highlighted by pH measurements and XRD experiments. To this purpose, spectra were collected at different times of hydration and analyzed by means of deconvolution in a region of interest, to follow the evolution of C-S-H formation. Fig. 4 shows the spectra of the freeze-dried powders collected at 0, 1, 3, 7, and 28 days. The increase of the intensities of the broad band centered at 3400 cm^{-1} and the small band at 1650 cm^{-1}, related to O-H stretching and bending, can be ascribed both to silanol groups and bound water [61,62], suggesting that the hydration process is proceeding for all the samples. The

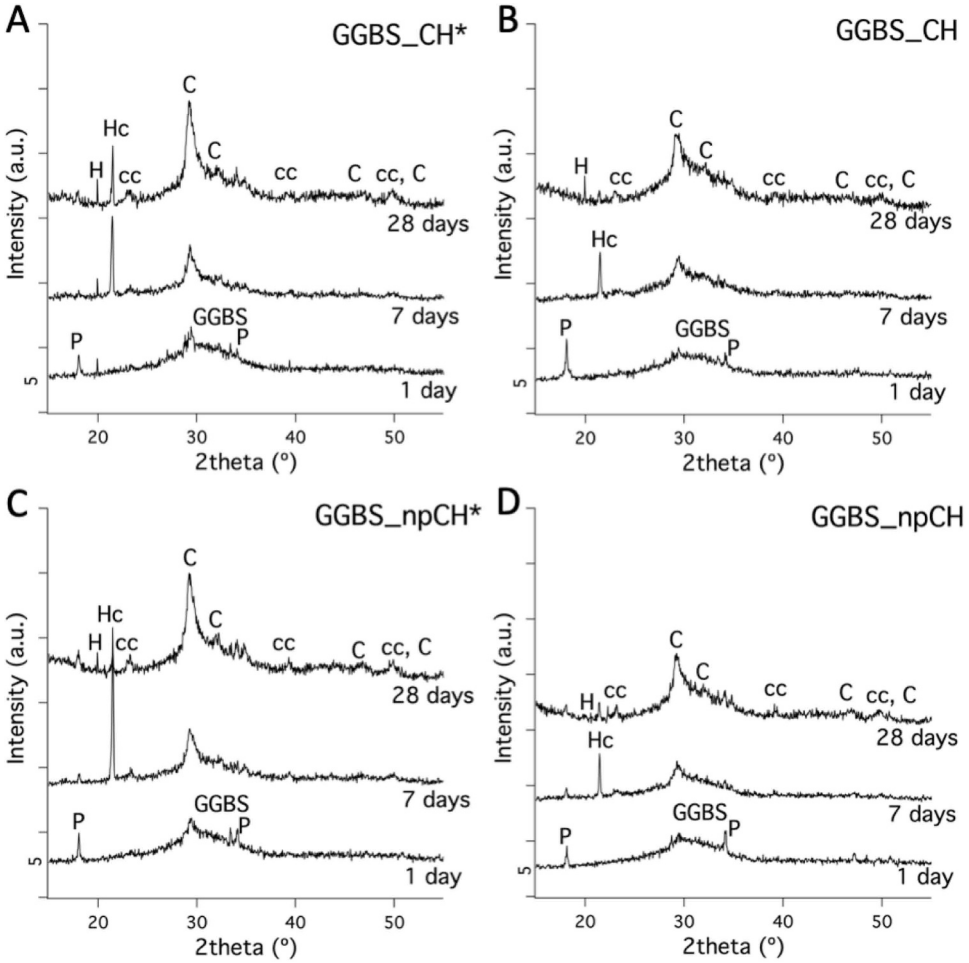

Fig. 3. XRD patterns of the investigated samples at different hydration times: GGBS_CH* (A), GGBS_CH (B), GGBS_npCH* (C), GGBS_npCH (D). P: portlandite (PDF 00–044–1481); H: hydrogarnet (PDF 01–076–0557); Hc: hemicarboaluminate (PDF 00–060–0312); cc: calcium carbonate (PDF 01–089–1304); C: C-S-H binder gel phase (PDF 00–006–0010).

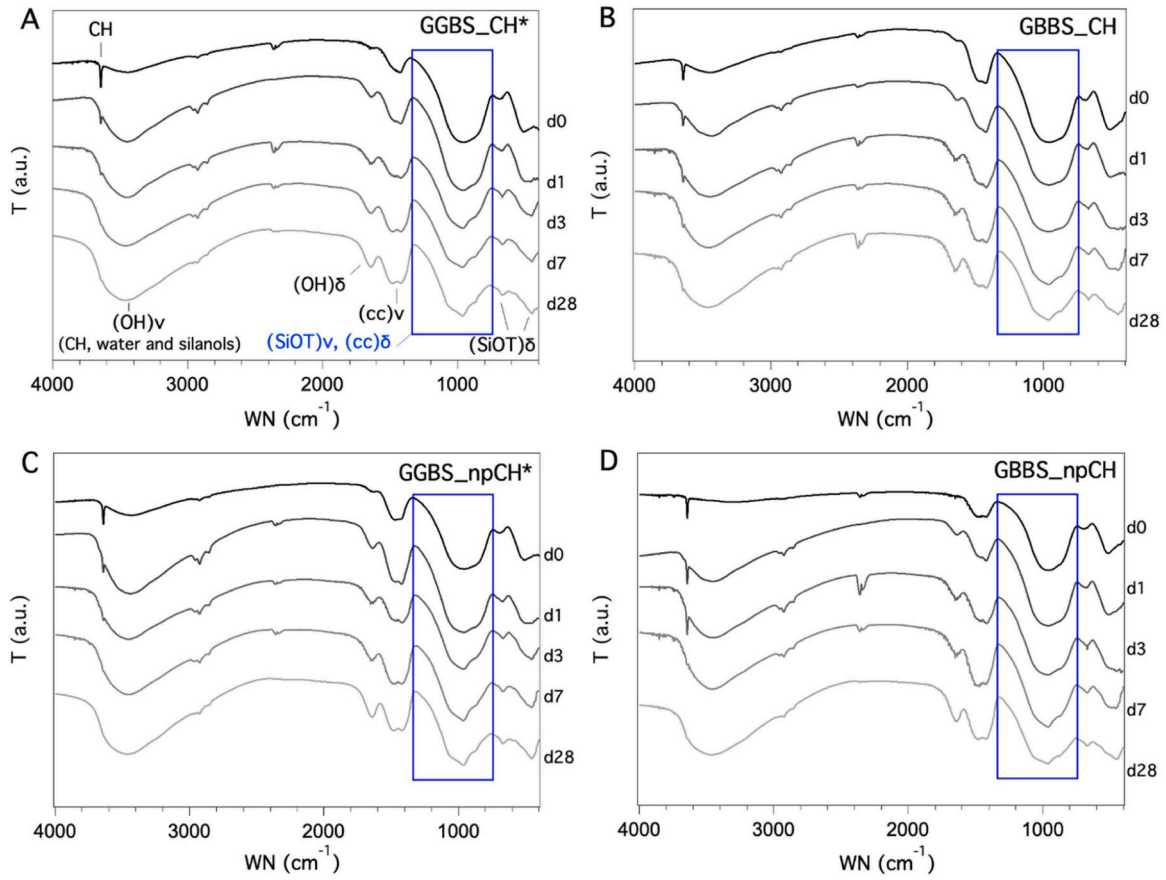

Fig. 4. Time evolution of the FT-IR spectra of the investigated formulations: A) GGBS_CH*, B) GGBS_CH, C) GGBS_npCH*, and D) GGBS_npCH. The blue box highlights the region of interest to monitor C-S-H formation.

characteristic absorption peak of portlandite, centered at 3642 cm^{-1} (O-H stretching) [63,64], decreases over time due to CH consumption in the pozzolanic reaction, as already observed in XRD diffractograms. A small amount of CH is still detected after 28 days only in GGBS_CH (see Fig. 4B), which could be regarded as the less reactive formulation. Some CH also inevitably transforms into calcium carbonate upon reaction with water and atmospheric CO_2, as testified by the broad band at 1400–1500 cm^{-1} (CO_3^{2-} asymmetric stretching, ν_3) and the signal at 870 cm^{-1} (CO_3^{2-} out-of-plane bending, ν_2) [63].

The signals in the 1200–400 cm^{-1} region are particularly interesting, being characteristic of symmetric and asymmetric stretching vibrations of Si–O–T bonds (where T = Si or Al) [52,61,65,66], and the group of bands between 1200 and 800 cm^{-1} can be used to gain information on the precipitation of C-S-H. According to the *dreierketten* model (see Fig. 5), C-S-H chains are constituted by repetitions of silica tetrahedra (Q^2 units), consisting in paired tetrahedra (Q^2_p units) facing the CaO interlayer, and bridging tetrahedra (Q^2_b units), with Q^1 species as terminal nuclei. In the investigated samples, the main band at 950–970 cm^{-1}, associated with T–O stretching modes of Q^2 tetrahedra, sharpens over time in all samples, along with the intensification of the shoulder at 1060–1070 cm^{-1}, related to stretching modes of Q^2 tetrahedra in bridging configuration, typical of C-S-H phases with Ca/Si > 1 [52,67]. The shoulder at 800–830 cm^{-1} is associated with stretching vibrations of Q^1 species, *i.e.*, dimers or ending tetrahedra, and it slightly changes shape over time, as also illustrated in the fitting analyses reported below (Fig. 5). Lastly, the region towards 1200 cm^{-1} is correlated to aluminosilicate stretching vibrations of highly condensed Q^3 silicates, where the bands' positions are reported to vary with aluminum content [66,68,69].

The small band at 670 cm^{-1}, present in all spectra, is assigned to Si–O–T bending, while the band at 400–500 cm^{-1} to TO_4 tetrahedra deformations. These peaks slightly change their shape with time in all samples, and can be ascribed either to the reactants (GGBS, see also Fig. S3 in the SM) or to the products of hydration.

To gain additional information about the evolution of C-S-H binder gel phase, the spectra were fitted in the 730–1330 cm^{-1} region (blue box in Fig. 4), as previously reported for the quantitative analyses of similar systems to study the deconvolution of the Si–O asymmetric and symmetric stretching bands in C–S–H gels [68]. A multipeak fitting analysis was performed using the minimum number of Gaussian peaks necessary for an accurate reconstruction and returned five contributions: (*i*) stretching of Q^1 tetrahedra at 815 cm^{-1}, (*ii*) carbonate bending at 865–870 cm^{-1}, (*iii*) stretching of Q^2 tetrahedra in pairing position (Q^2_p) at 950–955 cm^{-1}, (*iv*) stretching of Q^2 tetrahedra in bridging position (Q^2_b) at 1055–1060 cm^{-1}, and (*v*) stretching of Q^3 tetrahedra at 1150 cm^{-1}. Fig. 5 shows the curve fitting results for the GGBS_npCH* formulation, qualitatively representative of all CH-activated GGBS samples in the investigated conditions, reported in Fig. S4 in the SM. The broad distribution of Q_n species in the as-prepared formulations (time = 0 days) indicates a high degree of heterogeneity in the samples, originating from the dissolution of the original amorphous slag in the alkaline solution. As hydration proceeds, Q^1 signal decreases, along with a clear increase in the total amount of Q^2 units, indicating an enrichment in the silicate chains (number and length) over terminal tetrahedra or dimers, which is reported as fingerprint of the progressive re-arrangement into the typical *dreierketten chain* structure of C-S-H [70]. As a matter of fact, the C-S-H gel forming in alkali-activated systems resembles defective tobermorite crystals [71–73], in agreement with the XRD results.

The areas of the single Gaussian curves were also employed to

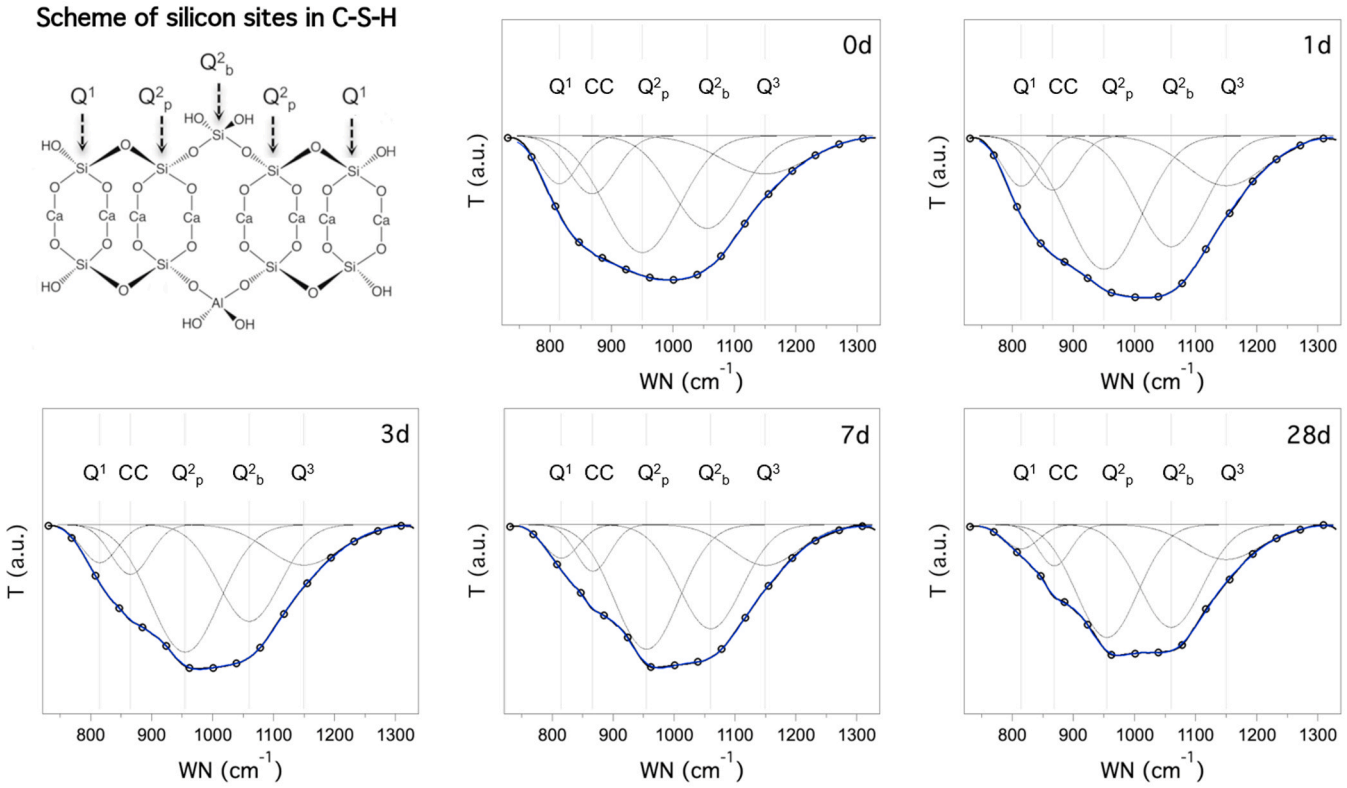

Fig. 5. Scheme of C-S-H structure, and deconvolution of FT-IR spectra of GGBS_npCH* formulation, in the Si–O–T symmetric and asymmetric stretching vibration region (730–1330 cm^{-1}), showing four contributions of Q_n aluminosilicate units and the contribution of calcium carbonate. Black markers represent the experimental data; blue lines are the global fitting curves, while the Gaussian peaks obtained by the fitting procedure are shown as dark gray curves.

quantitatively evaluate the hydration rate of the four formulations, by plotting the mean chain length (MCL = $2(1+Q_{2p}+Q_{2b})/(Q_1)$ [23]) as a function of time, as shown in Fig. 6. It is reasonable to speculate that the formation of new Q^2 sites, related with C-S-H growth, is associated with the loss of some Q^3 and Q^4 units of GGBS (as described in Fig. 1), favored by the presence of strong alkali that allow the dissolution of GGBS external layers to foster C-S-H formation. The presence of ethanol (samples GGBS_CH and GGBS_npCH) reduces the total amount of C-S-H gel that precipitates at the end of the investigated period of time (28 days), with respect to sole water formulations (GGBS_CH* and GGBS_npCH* systems). Moreover, a plateau is reached after about 7 days when ethanol is present. On the opposite, when sole water is present, MCL keeps increasing during the entire investigated period, indicating a continuous C-S-H growth. The observed behavior is due to the fact that organic liquids with low surface tension, like ethanol, can replace free water, which is a reactant, leading to a reduced precipitation of C-S-H. In particular, it is well known that ethanol can influence the hydration products by favoring the formation of carbonate like phases [74–76] and AFt phases (calcium aluminate ferrite) [77]. On the other hand, the use of nano-sized CH boosts the hydration rate at early stages, and after 1 month a larger amount of C-S-H is produced when using nano-CH with respect to the samples activated with bulk CH. Thus, FT-IR analysis proved that the high surface area of nano-CH not only accelerates and enhances the reaction rate at early stages, but also affects the total amount of C-S-H at later stages, as foreseen in the previous sections.

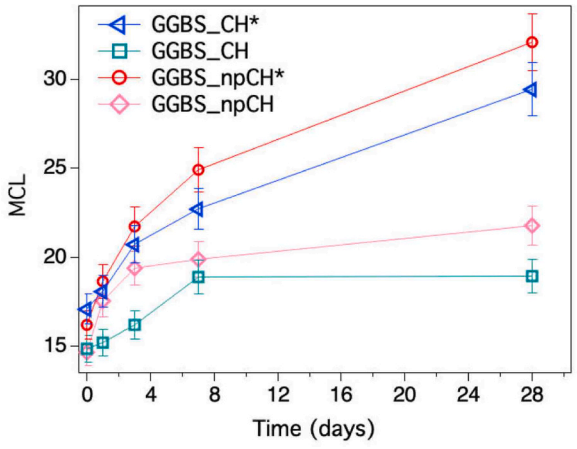

Fig. 6. Time plot of the mean chain length, obtained from the deconvolution of the FT-IR spectra of the four investigated formulations and calculated as MCL = $2(1 + Q_{2p} + Q_{2b})/(Q_1)$] [23].

SEM images were collected on the investigated formulations after 1, 7 and 28 days of reaction (see Fig. S5 in the SM), to monitor the morphological changes of the samples during hydration. The micrographs confirm the formation of abundant C-S-H, characterized by a morphology resembling nanofoils, which is expected to occur for Ca/Si ratios around or above 1.25 [78]. This result also agrees with pH and FT-IR experiments discussed above. Indeed, pH values measured at long hydration times, depending on C-S-H dissolution processes, were compatible with a binder gel phase described by a Ca/Si ratio of about 1.2 [50], while the appearance of the T–O stretching modes of the Q^2 tetrahedra in the FT-IR spectra suggested the presence of C-S-H phases described by Ca/Si > 1 [52,67]. In some samples, CH and $CaCO_3$ can be also identified, especially at short hydration times. The presence of unreacted portlandite and/or carbonate phases was already evidenced from FT-IR and XRD results, and it seems particularly abundant in the samples prepared using bulk CH, while in the formulations prepared with nano-CH no leftover portlandite was observed. SEM images of pure phases were collected as comparison, and are reported in Fig. S6 in the SM.

Following the results obtained from the thorough characterization of all formulations, we selected GGBS_npCH* as the most promising system to perform preliminary applications on adobe substrates: this is the formulation that allowed for the faster and the most abundant obtainment of C-S-H.

3.2. Characterization of the selected case study

GGBS_npCH* was prepared as described in Section 2.2, promptly applied on the surface of adobe mock-up samples (details in Section 2.4) and air cured for 28 days. In order to evaluate the consolidation efficiency of the treatment, the samples were characterized by means of different techniques. It is worth recalling that adobe is traditionally obtained from locally available materials, hence high variability can be found when comparing chemical and granulometric compositions of different earthen materials. Therefore, the selected adobe was here used as representative of a broad class of porous earthen materials, as preliminary tests on the compatibility and efficacy of the newly developed formulation.

First, 2D Confocal Raman mapping was used to investigate the precipitation of C-S-H on adobe surface, to confirm that the selected formulation allows for the obtainment of the desired binder gel phase also when applying the GGBS/npCH water dispersion on the surface of porous samples needing to be strengthen. Spectra of pristine phases were collected as reference, as reported in Fig. S7 in the SM. According to the results, due to their amorphous heterogeneous nature, GGBS and adobe do not show any particularly intense signal in the range of interest. Thus, the peak observed at 650 cm^{-1} in the consolidated substrates can be attributed to the presence of C-S-H, being associated to Q^2 stretching of the silicate chains [79,80]. The resulting maps are reported in Fig. 7, where the comparison between pristine and consolidated adobe is shown (Fig. 7A and B), together with representative spectra of the samples (Fig. 7C). The signal centered around 650 cm^{-1}, assigned to C-S-H and displayed in red, was used to obtain the confocal Raman maps reported in Fig. 7. As anticipated, the spectra collected on pristine adobe did not show any intense signal in the investigated conditions, probably due to the heterogeneity of amorphous phases that are present on the surface of the mock-up samples, despite the attempt to reduce the typical adobe roughness by using casted specimens (details in Section 2.4). On the contrary, the spectra acquired on consolidated samples (see Fig. 7C) display different signals in the investigated range: a peak centered at 310 cm^{-1} ascribed to Ca-O vibrations, a signal at 520 cm^{-1} due to deformations of Si-O tetrahedra, a peak at 610 cm^{-1} ascribed to Q^3 sites in the silicate chains, and peaks at 650 and 895 cm^{-1} ascribed to Q^3/Q^2 and Q^1 symmetrical stretching of C-S-H, respectively [52,79–81]. According to the results, C-S-H particles precipitated quite homogeneously on the surface of the treated adobe mock-up samples (see Fig. 7B), indicating that GGBS/npCH formulations can be used to efficiently consolidate earthen materials through the *in-situ* precipitation of this cementitious binder.

Once established that C-S-H formed on the surface of the air-cured adobe, we decided to investigate its penetration in the porous matrix, to evaluate the efficacy of the consolidation treatment. To this purpose, 3D computed X ray microtomography was used to monitor the pores variation before and after the treatment, as described in Section 2.5.2. According to the results, the use of GGBS_npCH* formulation allows for the consolidation of adobe, leading to a significant reduction of the porosity of such susceptible materials (see Table 2 and Fig. 8). In fact, the pristine mock-up sample displays a total porosity (TP) of about 10 %, which decreases up to 5 % after the treatment. To evaluate the depth at which the consolidation treatment has an effect, we performed an analysis of the obtained images, and we estimated the porosity of some sections at selected heights, both in the pristine and in the treated images (see Fig. 8B). Moreover, to visualize the changes occurring during the treatment, ascribed to the penetration of the dispersion and formation of C-S-H, the reconstructions were compared by overlapping some

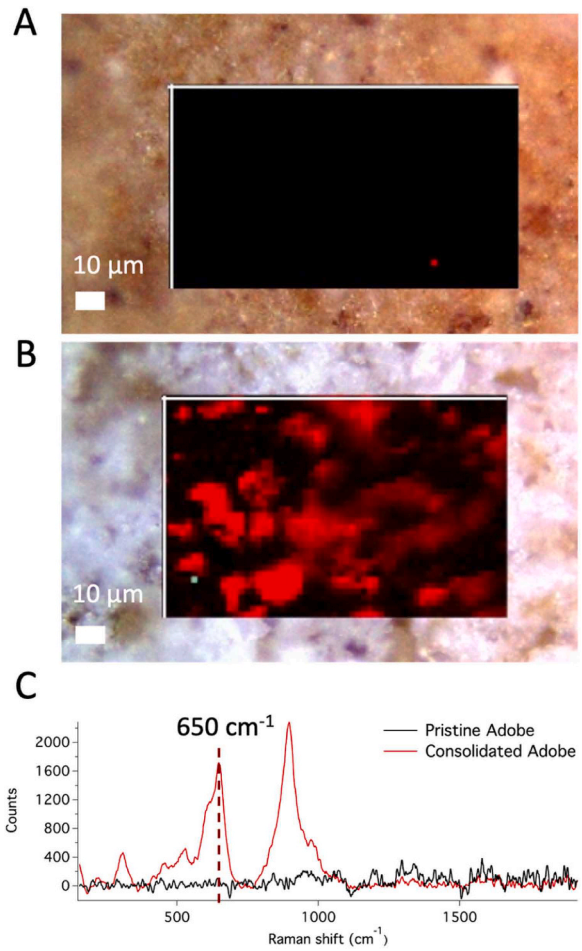

Fig. 7. Confocal Raman maps of pristine adobe mock-up sample (A) and treated adobe sample (B) where C-S-H signal at 650 cm^{-1} is displayed in red, together with representative spectra of the samples (C).

Table 2
Total porosity estimated using X-ray micro computed tomography. Total abrasion coefficient and decohesion index of pristine and consolidated adobe.

Sample	Total Porosity (%)	Total abrasion coefficient after 2 cycles (cm^2/g)	Decohesion index (mg/cm^2)
Pristine adobe	10	130 ± 21	0.75 ± 0.25
Treated adobe	5	247 ± 25	0.37 ± 0.02

2D sections of pristine and treated adobe. These comparisons allowed us to generate the so-called *difference images*, where one color is associated to the common regions shared by both images (*i.e.*, the regions where both images display the presence of material, blue areas in Fig. 8B), and another color is used to mark the difference between the two compared images (e.g., the regions where one image shows the presence of material, and the other image displays voids, purple areas in Fig. 8B). In our case, the *difference images* can be used to highlight the regions reached by the consolidation treatment, forming C-S-H, corresponding to the areas where the treated sample displays the presence of material, while the pristine adobe displays voids. Therefore, the regions colored in purple in Fig. 8B correspond to the presence of C-S-H binder that filled pores and cracks. According to the results, the treatment causes a decrease in the porosity in all the investigated 2D sections (max

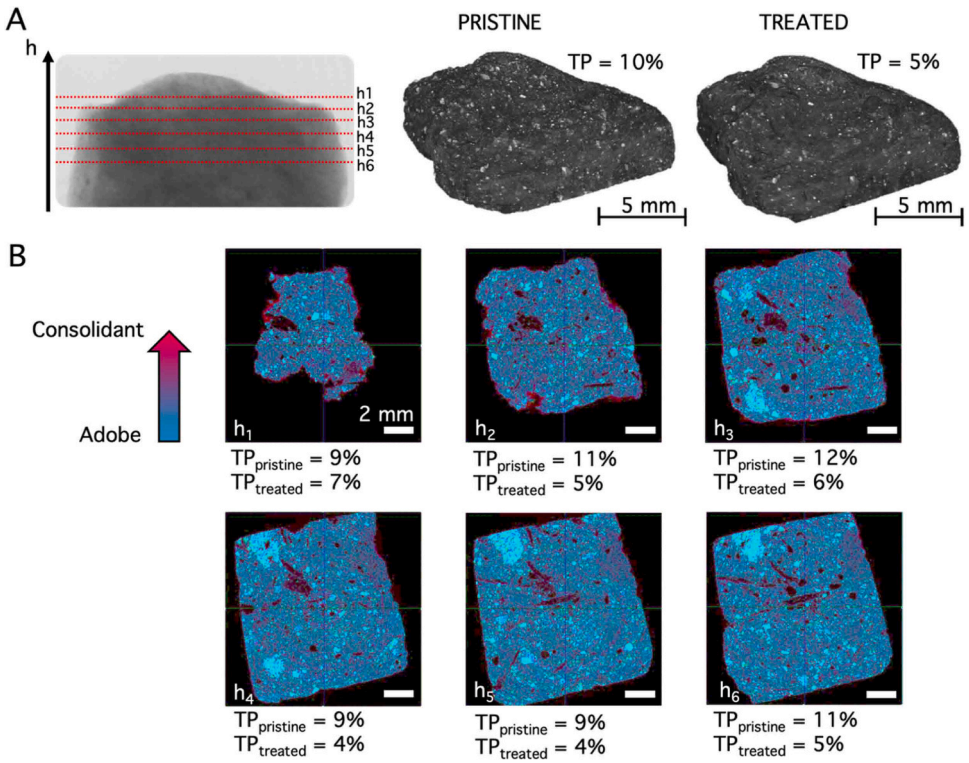

Fig. 8. (A) Optical image of the pristine sample where some selected heights are highlighted, together with the X-ray micro tomography 3D reconstruction images of pristine adobe before and after the treatment. (B) *Difference images* of 2D sections at selected heights, obtained by comparing sections of the pristine and treated adobe. The regions filled with C-S-H after the treatment (voids in the pristine sample) are colored in purple. The white scale bars correspond to 2 mm.

investigable depth ≈ 4 mm) and could be used for the consolidation of such permeable materials. In fact, despite the expected variability of TP values along the sample height ($TP_{pristine}$ ranges from 9 % to 12 %), the treated sample always displays lower values of porosity ($TP_{treated}$ ranges from 4 % to 7 %).

Further information about the effect of the consolidation treatment were obtained from abrasion and peeling tests, reported in Fig. 9 and Table 2. These tests are particularly indicated to evaluate the consolidation of adobe, since the damages that usually affect earthen-based materials first involve their surfaces, exposed to the external atmospheric agents. According to the results, the abrasion coefficient of adobe samples almost doubled after treatment with GGBS_npCH*, indicating that the treated samples gained an improved ability to withstand repetitive and wearing mechanical action, like scraping and rubbing. Fig. 9A shows the results of two abrasion cycles, indicating that the resistance was improved not only on the actual surface, but also on the layers below, as expected considering the X-ray micro tomography results. The average decohesion index obtained by peeling adhesive tapes from different areas of pristine and consolidated samples also resulted significantly reduced after treatment with GGBS_npCH* (see Fig. 9B). Thus, the material loss was strongly reduced after the application of the selected formulation, and the surface cohesion was restored. According to the results of the peeling tests, the treatment also produced a notable reduction of the standard deviation value, as reported in Table 2, highlighting a high variability of grains cohesiveness and compactness of untreated powdery adobe bricks, which is then flattened through consolidation. Fig. 9B also shows some pieces of adhesive tape removed from pristine and consolidated adobe: in the first case, the grains are widely and homogeneously removed from the surface, while in the second case only single grains are peeled off, highlighting the consolidating efficacy of the performed treatment on a highly powdery substrate.

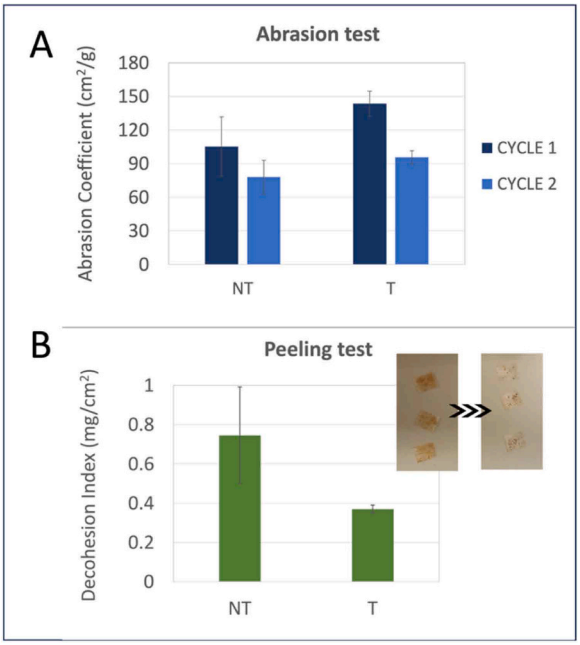

Fig. 9. Abrasion (A) and peeling (B) tests results for pristine (not treated, NT) and consolidated adobe (treated, T).

4. Conclusions

The consolidation of adobe is an age-old problem with broad impact. Among all possible solutions, the development of consolidation treatments based on the formation of C-S-H is particularly appropriate, being perfectly compatible with the substrates to be protected while allowing for the *in-situ* formation of the reinforcing phase.

The aim of this work was to investigate consolidation treatments

based on GGBS, a byproduct of the production of steel that is fully compatible with earthen based materials, activated with calcium hydroxide, towards the development of an effective and sustainable formulation for the reinforcement of adobe. To this purpose, different formulations were tested, containing fine GGBS, water and either bulk or nano-CH, in order to evaluate the effect of the granulometry of the activator, since alkali activators in the form of nanoparticles were never investigated so far. Taking into account that the synthesis of CH nanoparticles yields an ethanol dispersion, we decided also to test CH and nano-CH, both as a dry powder and as ethanol suspensions. The formulations were characterized by means of a multi-technique approach at different hydration times. Combining pH experiments with XRD, FT-IR, and SEM analyses we demonstrated that in all formulations abundant C-S-H binder gel phase was obtained, the most effective being the one prepared using dried nano-CH.

Following the promising results obtained from the thorough characterization of the dispersions, we selected the npCH/GGBS formulation to be applied on adobe mock-up samples, to assess its efficacy on the strengthening of such vulnerable materials. Confocal Raman maps confirmed the formation of abundant C-S-H binder within adobe porosities and cracks, while X-ray micro tomography revealed a reduction of the total porosity and demonstrated that the treatment can well penetrate through adobe matrix. Abrasion and peeling tests showed that the application of npCH/GGBS on earthen-based materials allowed for the obtainment of a better cohesion and improved ability to withstand mechanical action. Thus, abundant *in-situ* formation of C-S-H in the porous matrix of adobe confirmed that the consolidation process occurred. According to the results, we developed a novel formulation based on geopolymers as green cementitious binders activated by nano-CH for the consolidation of widespread earthen based materials. Future developments could include the use of different nano-sized activators, as well as the employment of this treatment for the consolidation of different porous substrates.

CRediT authorship contribution statement

Piero Baglioni: Writing – review & editing, Supervision. **Francesca Ridi:** Writing – review & editing, Supervision, Funding acquisition. **Monica Tonelli:** Writing – original draft, Methodology, Investigation, Conceptualization. **Rachel Camerini:** Writing – original draft, Methodology, Investigation, Conceptualization.

Declaration of Competing Interest

The authors declare that they have no known competing financial interests or personal relationships that could have appeared to influence the work reported in this paper.

Data availability

Data will be made available on request.

Acknowledgements

CSGI Consortium (Consorzio Interuniversitario per lo Sviluppo dei Sistemi a Grande Interfase), and MUR (“Progetto Dipartimenti di Eccellenza 2018–2022” allocated to Department of Chemistry “Ugo Schiff” and “Dipartimenti di Eccellenza 2023–2027” DICUS 2.0, University of Florence) are gratefully acknowledged for funding. The research was also funded under the National Recovery and Resilience Plan (NRRP), Mission 4 Component 2 “Dalla ricerca all’impresa” - Call for tender No. 341 of 15/03/2022 of Italian Ministry of Research funded by the European Union – NextGenerationEU, Project title “3A-ITALY - Made-in-Italy circolare e sostenibile.”, CUP: B83C22004890007.

All the authors gratefully acknowledge Dr. Yareli Jaidar (UNAM, Mexico City) for providing the adobe samples.

Ecocem is gratefully acknowledged for providing the ground granulated blast-furnace slag.

Dr. Samuele Ciattini and Dr. Laura Chelazzi (CRIST, University of Florence) are also gratefully acknowledged for their technical support with the X-ray micro computed tomography experiments and analyses.

Appendix A. Supporting information

Supplementary data associated with this article can be found in the online version at doi:10.1016/j.conbuildmat.2024.137285.

References

[1] E. Adorni, E. Coïsson, D. Ferretti, In situ characterization of archaeological adobe bricks, Constr. Build. Mater. 40 (2013) 1–9, https://doi.org/10.1016/j.conbuildmat.2012.11.004.
[2] P.W. Brown, J.R. Clifton, Adobe. I: the properties of adobe, Stud. Conserv. 23 (1978) 139–146, https://doi.org/10.2307/1505842.
[3] R. Camerini, D. Chelazzi, R. Giorgi, P. Baglioni, Hybrid nano-composites for the consolidation of earthen masonry, J. Colloid Interface Sci. 539 (2019) 504–515, https://doi.org/10.1016/j.jcis.2018.12.082.
[4] C. Galán-Marín, C. Rivera-Gómez, J. Petric, Clay-based composite stabilized with natural polymer and fibre, Constr. Build. Mater. 24 (2010) 1462–1468, https://doi.org/10.1016/j.conbuildmat.2010.01.008.
[5] P.Wencil Brown, C.R. Robbins, J.R. Clifton, ADOBE II: FACTORS AFFECTING THE DURABILITY OF ADOBE STRUCTURES: Studies in Conservation: Vol 24, No 1, Stud. Conserv. 24, 23–39. doi:10.2307/1505920.
[6] M. Hamiane, I. Djefour, H. Merabet, D. Bouallala, A. Zekagh, Y. Turki, M. Saidi, Design of adobe bricks of local raw materials for use in the monuments of earthen architecture, Civ. Eng. Archit. 4 (2016) 147–152, https://doi.org/10.13189/cea.2016.040401.
[7] J.R. Clifton, Preservation of historic adobe structures: a status report, Department of Commerce, National Bureau of Standards, Institute for Applied Technology, 1977. ⟨https://onlinebooks.library.upenn.edu/webbin/book/lookupid?key=ha009487848⟩.
[8] G. Wheeler, Alkoxysilanes and the Consolidation of Stone. Research in Conservation, Getty Conservation Institute, Los Angeles, 2005. ⟨http://hdl.handle.net/10020/gci_pubs/consolidation_of_stone⟩.
[9] A.P.F. Pinto, J.D. Rodrigues, Stone consolidation: the role of treatment procedures - ScienceDirect, J. Cult. Herit. 9 (2008) 38–53, https://doi.org/10.1016/j.culher.2007.06.004.
[10] F. Ridi, M. Tonelli, E. Fratini, S.-H. Chen, P. Baglioni, Water as a probe of the colloidal properties of cement, Langmuir 34 (2018) 2205–2218, https://doi.org/10.1021/acs.langmuir.7b02304.
[11] M. Burgos-Ruiz, K. Elert, E. Ruiz-Agudo, H. Cölfen, C. Rodriguez-Navarro, Silica-functionalized nanolimes for the conservation of stone heritage, Small 19 (2023) 2300596, https://doi.org/10.1002/smll.202300596.
[12] R. Zarzuela, M. Luna, L.M. Carrascosa, M.P. Yeste, I. Garcia-Lodeiro, M.T. Blanco-Varela, M.A. Cauqui, J.M. Rodríguez-Izquierdo, M.J. Mosquera, Producing C-S-H gel by reaction between silica oligomers and portlandite: a promising approach to repair cementitious materials, Cem. Concr. Res. 130 (2020) 106008, https://doi.org/10.1016/j.cemconres.2020.106008.
[13] B. Lothenbach, K. Scrivener, R.D. Hooton, Supplementary cementitious materials, Cem. Concr. Res. 41 (2011) 1244–1256, https://doi.org/10.1016/j.cemconres.2010.12.001.
[14] H.A. Colorado, E.I.G. Velásquez, S.N. Monteiro, Sustainability of additive manufacturing: the circular economy of materials and environmental perspectives, J. Mater. Res. Technol. 9 (2020) 8221–8234, https://doi.org/10.1016/j.jmrt.2020.04.062.
[15] M. Tonelli, F. Martini, L. Calucci, E. Fratini, M. Geppi, F. Ridi, S. Borsacchi, P. Baglioni, Structural characterization of magnesium silicate hydrate: towards the design of eco-sustainable cements, Dalton Trans. 45 (2016) 3294–3304, https://doi.org/10.1039/C5DT03545G.
[16] E. Özbay, M. Erdemir, H.İ. Durmuş, Utilization and efficiency of ground granulated blast furnace slag on concrete properties – a review, Constr. Build. Mater. 105 (2016) 423–434, https://doi.org/10.1016/j.conbuildmat.2015.12.153.
[17] R. James, A.H.M. Kamruzzaman, A. Haque, A. Wilkinson, Behaviour of lime–slag-treated clay, Proc. Inst. Civ. Eng. - Ground Improv. 161 (2008) 207–216, https://doi.org/10.1680/grim.2008.161.4.207.
[18] J.M. Kinuthia, J.E. Oti, Designed non-fired clay mixes for sustainable and low carbon use, Appl. Clay Sci. 59–60 (2012) 131–139, https://doi.org/10.1016/j.clay.2012.02.021.
[19] G. Ding, J. Xu, Y. Wei, R. Chen, X. Li, Engineered reclamation fill material created from excavated soft material and granulated blast furnace slag - ScienceDirect, Resour. Conserv. Recycl. 150 (2019) 104428, https://doi.org/10.1016/j.resconrec.2019.104428.
[20] S.C. Pal, A. Mukherjee, S.R. Pathak, Investigation of hydraulic activity of ground granulated blast furnace slag in concrete, Cem. Concr. Res. 33 (2003) 1481–1486, https://doi.org/10.1016/S0008-8846(03)00062-0.
[21] L. Ting, W. Qiang, Z. Shiyu, Effects of ultra-fine ground granulated blast-furnace slag on initial setting time, fluidity and rheological properties of cement pastes,

Powder Technol. 345 (2019) 54–63, https://doi.org/10.1016/j.powtec.2018.12.094.
[22] A.J. Allen, J.J. Thomas, H.M. Jennings, Composition and density of nanoscale calcium–silicate–hydrate in cement, Nat. Mater. 6 (2007) 311–316, https://doi.org/10.1038/nmat1871.
[23] F. Martini, M. Tonelli, M. Geppi, F. Ridi, S. Borsacchi, L. Calucci, Hydration of MgO/SiO_2 and Portland cement mixtures: a structural investigation of the hydrated phases by means of X-ray diffraction and solid state NMR spectroscopy, Cem. Concr. Res. (2017), https://doi.org/10.1016/j.cemconres.2017.08.029.
[24] C.B. Cheah, L.E. Tan, M. Ramli, Recent advances in slag-based binder and chemical activators derived from industrial by-products – a review, Constr. Build. Mater. 272 (2021) 121657, https://doi.org/10.1016/j.conbuildmat.2020.121657.
[25] S. Song, D. Sohn, H.M. Jennings, T.O. Mason, Hydration of alkali-activated ground granulated blast furnace slag, J. Mater. Sci. 35 (n.d.) 249–257. doi:10.1023/A:1004742027117.
[26] S. Song, H.M. Jennings, Pore solution chemistry of alkali-activated ground granulated blast-furnace slag, Cem. Concr. Res. 29 (1999) 159–170, https://doi.org/10.1016/S0008-8846(98)00212-9.
[27] D. Law, J. Evans, Effect of leaching on ph of surrounding water, Mag. Concr. Res. 110 (2013) 291–296, https://doi.org/10.14359/51685662.
[28] V. Daniele, G. Taglieri, Synthesis of $Ca(OH)_2$ nanoparticles with the addition of Triton X-100. Protective treatments on natural stones: preliminary results, J. Cult. Herit. 13 (2012) 40–46, https://doi.org/10.1016/j.culher.2011.05.007.
[29] A. Naji Givi, S. Abdul Rashid, F.N.A. Aziz, M.A.M. Salleh, The effects of lime solution on the properties of SiO_2 nanoparticles binary blended concrete, Compos. Part B Eng. 42 (2011) 562–569, https://doi.org/10.1016/j.compositesb.2010.10.002.
[30] D. Chelazzi, P. Baglioni, From nanoparticles to gels: a breakthrough in art conservation science, Langmuir 39 (2023) 10744–10755, https://doi.org/10.1021/acs.langmuir.3c01324.
[31] P. Baglioni, R. Giorgi, Soft and hard nanomaterials for restoration and conservation of cultural heritage, Soft Matter 2 (2006) 293–303, https://doi.org/10.1039/B516442G.
[32] D. Chelazzi, G. Poggi, Y. Jaidar, N. Toccafondi, R. Giorgi, P. Baglioni, Hydroxide nanoparticles for cultural heritage: consolidation and protection of wall paintings and carbonate materials - ScienceDirect, J. Colloid Interface Sci. 392 (2013) 42–49, https://doi.org/10.1016/j.jcis.2012.09.069.
[33] M. Brun, A. Lallemand, J.-F. Quinson, C. Eyraud, A new method for the simultaneous determination of the size and shape of pores: the thermoporometry, Thermochim. Acta 21 (1977) 59–88, https://doi.org/10.1016/0040-6031(77)85122-8.
[34] R. Camerini, G. Poggi, F. Ridi, P. Baglioni, The kinetic of calcium silicate hydrate formation from silica and calcium hydroxide nanoparticles, J. Colloid Interface Sci. 605 (2022) 33–43, https://doi.org/10.1016/j.jcis.2021.06.168.
[35] G. Poggi, N. Toccafondi, L.N. Melita, J.C. Knowles, L. Bozec, R. Giorgi, P. Baglioni, Calcium hydroxide nanoparticles for the conservation of cultural heritage: new formulations for the deacidification of cellulose-based artifacts, Appl. Phys. A. 114 (2014) 685–693, https://doi.org/10.1007/s00339-013-8172-7.
[36] G. Poggi, N. Toccafondi, D. Chelazzi, P. Canton, R. Giorgi, P. Baglioni, Calcium hydroxide nanoparticles from solvothermal reaction for the deacidification of degraded waterlogged wood, J. Colloid Interface Sci. 473 (2016) 1–8, https://doi.org/10.1016/j.jcis.2016.03.038.
[37] S. Song, H.M. Jennings, Pore solution chemistry of alkali-activated ground granulated blast-furnace slag, Cem. Concr. Res. 29 (1999) 159–170, https://doi.org/10.1016/S0008-8846(98)00212-9.
[38] T. Zhang, L.J. Vandeperre, C.R. Cheeseman, Formation of magnesium silicate hydrate (M-S-H) cement pastes using sodium hexametaphosphate, Cem. Concr. Res. 65 (2014) 8–14, https://doi.org/10.1016/j.cemconres.2014.07.001.
[39] R. Gelli, M. Tonelli, F. Martini, L. Calucci, S. Borsacchi, F. Ridi, Effect of borax on the hydration and setting of magnesium phosphate cements, Constr. Build. Mater. 348 (2022) 128686, https://doi.org/10.1016/j.conbuildmat.2022.128686.
[40] AFNOR - XP P13–901 - Compressed earth blocks fo walls and partitions: definitions - Specifications - Test methods - Delivery acceptance conditions, (2001). https://standards.globalspec.com/std/811579/XP%20P13–901
[41] O. Izemmouren, A. Guettala, S. Guettala, Mechanical properties and durability of lime and natural pozzolana stabilized steam-cured compressed earth block bricks, Geotech. Geol. Eng. 33 (2015) 1321–1333, https://doi.org/10.1007/s10706-015-9904-6.
[42] M. Drdácký, J. Lesák, S. Rescic, Z. Slížková, P. Tiano, J. Valach, Standardization of peeling tests for assessing the cohesion and consolidation characteristics of historic stone surfaces, Mater. Struct. 45 (2012) 505–520, https://doi.org/10.1617/s11527-011-9778-x.
[43] E. Bernard, B. Lothenbach, F. Le Goff, I. Pochard, A. Dauzères, Effect of magnesium on calcium silicate hydrate (C-S-H), Cem. Concr. Res. 97 (2017) 61–72, https://doi.org/10.1016/j.cemconres.2017.03.012.
[44] M. Tonelli, F. Martini, L. Calucci, M. Geppi, S. Borsacchi, F. Ridi, Traditional Portland cement and MgO-based cement: a promising combination? Phys. Chem. Earth Parts ABC 99 (2017) 158–167, https://doi.org/10.1016/j.pce.2017.01.011.
[45] S.A. Greenberg, T.N. Chang, E. Anderson, Investigation of colloidal hydrated calcium silicates. I. Solubility products, J. Phys. Chem. 64 (1960) 1151–1157, https://doi.org/10.1021/j100838a012.
[46] J.J. Chang, A study on the setting characteristics of sodium silicate-activated slag pastes, Cem. Concr. Res. 33 (2003) 1005–1011, https://doi.org/10.1016/S0008-8846(02)01096-7.
[47] E. Deir, B.S. Gebregziabiher, S. Peethamparan, Influence of starting material on the early age hydration kinetics, microstructure and composition of binding gel in alkali activated binder systems, Cem. Concr. Compos. 48 (2014) 108–117, https://doi.org/10.1016/j.cemconcomp.2013.11.010.
[48] Q. Lin, Z. Xu, X. Lan, Y. Ni, C. Lu, The reactivity of nano silica with calcium hydroxide, J. Biomed. Mater. Res. B Appl. Biomater. 99B (2011) 239–246, https://doi.org/10.1002/jbm.b.31891.
[49] G.M.N. Baston, A.P. Clacher, T.G. Heath, F.M.I. Hunter, V. Smith, S.W. Swanton, Calcium silicate hydrate (C-S-H) gel dissolution and pH buffering in a cementitious near field, Mineral. Mag. 76 (2012) 3045–3053, https://doi.org/10.1180/minmag.2012.076.8.20.
[50] W.B. Euler, L.J. Kirschenbaum, B. Ruekberg, Determination of Ksp, ΔG0, ΔH0, and ΔS0, Chem. Educ. 77 (8) (2000), https://doi.org/10.1021/ed077p1039.
[51] T. Zhang, C.R. Cheeseman, L.J. Vandeperre, Development of low pH cement systems forming magnesium silicate hydrate (M-S-H), Cem. Concr. Res. 41 (2011) 439–442, https://doi.org/10.1016/j.cemconres.2011.01.016.
[52] Y. Yan, S.-Y. Yang, G.D. Miron, I.E. Collings, E. L'Hôpital, J. Skibsted, F. Winnefeld, K. Scrivener, B. Lothenbach, Effect of alkali hydroxide on calcium silicate hydrate (C-S-H), Cem. Concr. Res. 151 (2022) 106636, https://doi.org/10.1016/j.cemconres.2021.106636.
[53] M. Ben Haha, G. Le Saout, F. Winnefeld, B. Lothenbach, Influence of activator type on hydration kinetics, hydrate assemblage and microstructural development of alkali activated blast-furnace slags, Cem. Concr. Res. 41 (2011) 301–310, https://doi.org/10.1016/j.cemconres.2010.11.016.
[54] M.S. Kim, Y. Jun, C. Lee, J.E. Oh, Use of CaO as an activator for producing a price-competitive non-cement structural binder using ground granulated blast furnace slag, Cem. Concr. Res. 54 (2013) 208–214, https://doi.org/10.1016/j.cemconres.2013.09.011.
[55] K.-H. Yang, A.-R. Cho, J.-K. Song, S.-H. Nam, Hydration products and strength development of calcium hydroxide-based alkali-activated slag mortars, Constr. Build. Mater. 29 (2012) 410–419, https://doi.org/10.1016/j.conbuildmat.2011.10.063.
[56] Y.A. Criado, J.C. Abanades, Carbonation rates of dry $Ca(OH)_2$ mortars for CO_2 capture applications at ambient temperatures, Ind. Eng. Chem. Res. 61 (2022) 14804–14812, https://doi.org/10.1021/acs.iecr.2c01675.
[57] T. Matschei, B. Lothenbach, F.P. Glasser, The AFm phase in Portland cement, Cem. Concr. Res. 37 (2007) 118–130, https://doi.org/10.1016/j.cemconres.2006.10.010.
[58] H. Huang, G. Ye, D. Damidot, Effect of blast furnace slag on self-healing of microcracks in cementitious materials, Cem. Concr. Res. 60 (2014) 68–82, https://doi.org/10.1016/j.cemconres.2014.03.010.
[59] B.Z. Dilnesa, B. Lothenbach, G. Renaudin, A. Wichser, D. Kulik, Synthesis and characterization of hydrogarnet $Ca_3(Al_xFe_{1-x})_2(SiO_4)_y(OH)_{4(3-y)}$, Cem. Concr. Res. 59 (2014) 96–111, https://doi.org/10.1016/j.cemconres.2014.02.001.
[60] A.B. Tchamba, J.C. Sofack, R. Yongue, U.C. Melo, Formulation of calcium dialuminate ($CaO{\cdot}2Al_2O_3$) refractory cement from local bauxite, J. Asian Ceram. Soc. 3 (2015) 164–172, https://doi.org/10.1016/j.jascer.2015.01.001.
[61] P. Yu, R.J. Kirkpatrick, B. Poe, P.F. McMillan, X. Cong, Structure of calcium silicate hydrate (C-S-H): Near-, Mid-, and Far-infrared spectroscopy, J. Am. Ceram. Soc. 82 (1999) 742–748, https://doi.org/10.1111/j.1151-2916.1999.tb01826.x.
[62] A. Aboulayt, F. Souayfan, E. Roziere, R. Jaafri, A. Cherki El Idrissi, R. Moussa, C. Justino, A. Loukili, Alkali-activated grouts based on slag-fly ash mixtures: From early-age characterization to long-term phase composition, Constr. Build. Mater. 260 (2020) 120510, https://doi.org/10.1016/j.conbuildmat.2020.120510.
[63] F.A. Andersen, L. Brecevic, Infrared spectra of amorphous and crystalline calcium carbonate, ACTA Chem. Scand. (1991) 1018–1024, https://doi.org/10.3891/acta.chem.scand.45-1018.
[64] R. Camerini, G. Poggi, D. Chelazzi, F. Ridi, R. Giorgi, P. Baglioni, The carbonation kinetics of calcium hydroxide nanoparticles: a boundary nucleation and growth description, J. Colloid Interface Sci. 547 (2019) 370–381, https://doi.org/10.1016/j.jcis.2019.03.089.
[65] Y. Yan, B. Ma, G.D. Miron, D.A. Kulik, K. Scrivener, B. Lothenbach, Al uptake in calcium silicate hydrate and the effect of alkali hydroxide, Cem. Concr. Res. 162 (2022) 106957, https://doi.org/10.1016/j.cemconres.2022.106957.
[66] B. Lothenbach, D. Jansen, Y. Yan, J. Schreiner, Solubility and characterization of synthesized 11 Å Al-tobermorite, Cem. Concr. Res. 159 (2022) 106871, https://doi.org/10.1016/j.cemconres.2022.106871.
[67] R. Caron, R.A. Patel, G.D. Miron, C. Le Galliard, B. Lothenbach, F. Dehn, Microstructure development of slag activated with sodium silicate solution: experimental characterization and thermodynamic modeling, J. Build. Eng. 71 (2023) 106398, https://doi.org/10.1016/j.jobe.2023.106398.
[68] I.F. Sáez del Bosque, S. Martínez-Ramírez, M.T. Blanco-Varela, FTIR study of the effect of temperature and nanosilica on the nano structure of C-S-H gel formed by hydrating tricalcium silicate, Constr. Build. Mater. 52 (2014) 314–323, https://doi.org/10.1016/j.conbuildmat.2013.10.056.
[69] X. Qu, Z. Zhao, X. Zhao, Microstructure and characterization of aluminum-incorporated calcium silicate hydrates (C-S-H) under hydrothermal conditions, RSC Adv. 8 (2018) 28198–28208, https://doi.org/10.1039/C8RA04423F.
[70] A.I. Ruiz, E. Reyes, C. Argiz, M.A. de la Rubia, A. Moragues, Nano-scale aluminium interaction in synthetic hydrated calcium silicate gel studied by 29Si MAS NMR, Bol. Soc. Esp. Cerámica Vidr. 62 (2023) 388–401, https://doi.org/10.1016/j.bsecv.2022.06.004.
[71] H.F.W. Taylor. Cement chemistry, 2nd ed, T. Telford, London, 1997.
[72] X. Cong, R.J. Kirkpatrick, 29Si MAS NMR study of the structure of calcium silicate hydrate, Adv. Cem. Based Mater. 3 (1996) 144–156, https://doi.org/10.1016/S1065-7355(96)90046-2.

[73] X. Hou, R.J. Kirkpatrick, L.J. Struble, P.J.M. Monteiro, Structural Investigations of Alkali Silicate Gels, J. Am. Ceram. Soc. 88 (2005) 943–949, https://doi.org/10.1111/j.1551-2916.2005.00145.x.
[74] K.S. Lothenbach Ruben Snellings, Barbara (Eds.), A Practical Guide to Microstructural Analysis of Cementitious Materials, CRC Press, Boca Raton, 2017, https://doi.org/10.1201/b19074.
[75] E. Knapen, O. Cizer, K. Van Balen, D. Van Gemert, Effect of free water removal from early-age hydrated cement pastes on thermal analysis, Constr. Build. Mater. 23 (2009) 3431–3438, https://doi.org/10.1016/j.conbuildmat.2009.06.004.
[76] J. Zhang, G.W. Scherer, Comparison of methods for arresting hydration of cement, Cem. Concr. Res. 41 (2011) 1024–1036, https://doi.org/10.1016/j.cemconres.2011.06.003.
[77] A. Mezhov, D. Kulisch, A. Goncharov, S. Zhutovsky, A comparative study of factors influencing hydration stoppage of hardened cement paste, Sustainability 15 (2023) 1080, https://doi.org/10.3390/su15021080.
[78] A. Kumar, B.J. Walder, A. Kunhi Mohamed, A. Hofstetter, B. Srinivasan, A. J. Rossini, K. Scrivener, L. Emsley, P. Bowen, The atomic-level structure of cementitious calcium silicate hydrate, J. Phys. Chem. C 121 (2017) 17188–17196, https://doi.org/10.1021/acs.jpcc.7b02439.
[79] R.J. Kirkpatrick, J.L. Yarger, P.F. McMillan, Y. Ping, X. Cong, Raman spectroscopy of C-S-H, tobermorite, and jennite, Adv. Cem. Based Mater. 5 (1997) 93–99, https://doi.org/10.1016/S1065-7355(97)00001-1.
[80] D.W. Gardner, J. Li, A. Morshedifard, S. Masoumi, M.J. Abdolhosseini Qomi, P.J. M. Monteiro, R. Maboudian, C. Carraro, Silicate bond characteristics in calcium–silicate–hydrates determined by high pressure Raman spectroscopy, J. Phys. Chem. C 124 (2020) 18335–18345, https://doi.org/10.1021/acs.jpcc.0c04563.
[81] S. Ortaboy, J. Li, G. Geng, R.J. Myers, P.J.M. Monteiro, R. Maboudian, C. Carraro, Effects of CO_2 and temperature on the structure and chemistry of C-(A-)S-H investigated by Raman spectroscopy, RSC Adv. 7 (2017) 48925–48933, https://doi.org/10.1039/C7RA07266J.